Energy Storage Materials 50 (2022) 365–372

Contents lists available at ScienceDirect

Energy Storage Materials

journal homepage: www.elsevier.com/locate/ensm

Heterogeneous stacking carbon films for optimized supercapacitor performance

Xiaoli Su, Chuanren Ye, Xinpeng Li, Minghao Guo, Ruiguo Cao, Kun Ni *, Yanwu Zhu *

Department of Materials Science and Engineering, School of Chemistry and Materials Science, University of Science and Technology of China, Hefei 230026, Anhui, China

ARTICLE INFO

Keywords:
Heterogeneous stacking carbon films
Supercacitor
Pore features
Stacking orders
Ionic transport

ABSTRACT

Porous carbons are widely used as electrode materials for supercapacitors but the further increase in the performance is restricted by the challenge of tuning the porosity in the single type of carbons. The deteriorated ionic dynamics is a bottleneck for thick or high-mass-loading electrodes in the practical applications, requiring a rational design of electrodes. Herein, we demonstrate that, by simply stacking films made of carbons with differential pore features, the specific capacitance and ionic transport can be optimized based on the stacking order in the electrodes. Specifically, we find out that reduced graphene oxide (rGO) with large mesopores can efficiently improve the ionic transport when being placed in the middle, which is further supported by the finite element and molecular dynamics simulations. When an activated carbon YP50F, rGO and activated microwave exfoliated graphite oxide (aMEGO) are sequentially stacked with aMEGO nearby the separator, a high loading (~210 μm, ~10 mg, ~12.7 mg cm^{-2}) of active materials in the electrode delivers the higher capacitances (171.4 F g^{-1}, 102.8 F cm^{-3}, 2.2 F cm^{-2}) compared to other stacking orders or single types of electrodes, in an electrolyte of ionic liquid in acetonitrile at a voltage of 2.7 V.

1. Introduction

Owing to high power density, long life-span and fast charge/discharge rate, supercapacitors such as electric double layer capacitors (EDLCs) have drawn much attention [1–3]. Nowadays, most of the commercial EDLCs are assembled based on carbon electrodes operated in organic electrolytes [4]. With decades of research, one has realized that the small pores in the EDLC electrode with size close to the ion size contribute to the capacitance mainly via adsorption/desorption, while the large pores act as an ion buffer for ion transport [5, 6]. To improve the specific capacitance, numerous research work has been directed to increase the pore volume and/or specific surface area (SSA), *e.g.*, through various activation strategies [7–9]. However, high SSA and well-developed pores may lower the mass density of the electrode, and thus deteriorate the volumetric and areal capacitance, leading to practically less useful device merits [10,11]. To meet the requirement in practical applications, several pore engineering strategies have been carried out to successfully enhance the capacitance of high-mass-loading electrodes [12, 13]. For instance, Li et al. prepared graphene-based monoliths showing a SSA of 891 m^2 g^{-1} and a density of 0.87 g cm^{-3} using $ZnCl_2$ activation and capillary drying [14], which were used to fabricate a 400 μm-thick electrode with a volumetric capacitance of 150 F cm^{-3}. Kim et al. developed a spray-drying method for the preparation of graphene powder with a density of 1.4 g cm^{-3} and a SSA of 182 m^2 g^{-1}, displaying a volumetric capacitance of 259 F cm^{-3} [15]. Li et al. reported freestanding graphene films by precisely adjusting the interlayer spacing, which exhibited SSAs from 35 to 612 m^2 g^{-1} and densities from 1.51 to 0.70 g cm^{-3}; the as-fabricated EDLCs made of such films show an impressive volumetric capacitance up to 203 F cm^{-3} [16].

In thick or high-mass-loading electrodes, charge/discharge is heavily restricted by ionic dynamics during adsorption/desorption of ions [17]. In an experiment using carbide-derived carbon (CDC) as the electrode, the capacitance decreased when the pore size was reduced till a critical value of ~1 nm, and then sharply increased, which was presumably attributed to the partial removal of solvation shell of ions in the pores with size close to the ion size [18–20]. In another study, Gao et al. developed a heterogeneous membrane consisting of negatively charged mesoporous carbon and positively charged macroporous alumina [21], from which a suppression of ion concentration polarization at low concentrations was observed, consequently promoting the overall power performance. The more efficient ionic transport was attributed to the asymmetry of structure, chemical composition and surface charge

* Corresponding authors.
E-mail addresses: nikun@ustc.edu.cn (K. Ni), zhuyanwu@ustc.edu.cn (Y. Zhu).

https://doi.org/10.1016/j.ensm.2022.05.020
Received 1 December 2021; Received in revised form 24 April 2022; Accepted 12 May 2022
Available online 14 May 2022

polarity, which was further verified by an experiment designed using three-layer stacking graphene membranes with different pore sizes along the thickness direction [22]. It was found that the inner layers in the gradient structure stored more charges than the uniform structure and ions could diffuse more easily into the thickness direction in the gradient electrode.

Clearly, the heterogeneous structure in electrodes could provide more opportunities to regulate the ionic behaviors in the structure, which deserves more research attention. In observation of the complications for creating gradient structure in single type of carbons [23], assembling carbons with differential pore features in a stacking would be a straightforward way to obtain such heterogeneous electrodes, which also allows one to understand the ionic behavior through the interfaces in the stacking. Among a large variety of electrode materials, three widely used carbons while with clearly different pore features have drawn our attention. Activated carbon such as YP50F is a commercial active material in EDLCs because of relatively low costs, high SSA ($> 2000\ m^2\ g^{-1}$) and good conductivity [4, 24]. Graphene-derived carbons, such as reduced graphene oxide (rGO) own superior electrical conductivity due to the two-dimensional feature of the structural unit while with a relatively low SSA ($< 1000\ m^2\ g^{-1}$) [25, 26]. On the other hand, activated microwave exfoliated graphene oxide (aMEGO) has a reported SSA of $> 3000\ m^2\ g^{-1}$ made by restructuring of graphene platelets with KOH activation [27, 28]. We expect that the combination of these three carbons would give us a hint on the rational design of heterogeneous stacking electrodes, providing opportunities to achieve the higher performance of high-mass-loading electrodes.

Herein, YP50F, rGO and aMEGO have been selected as the model materials for the design of heterogeneous electrodes. When electrode films made of these carbons are stacked to form thicker electrodes, we find the charge storage performance is sensitive to the stacking order of these films along the thickness direction. Specifically, we identify the role of rGO and aMEGO in the stacking as an ion transport channel and an ion storage medium, respectively. Based on such understanding, the three-layer stacking electrode of YP50F, rGO and aMEGO with aMEGO nearby the separator demonstrates the optimized capacitance of ~210 μm thick electrode with a density of ~0.61 g cm^{-3} in an ionic liquid electrolyte in acetonitrile.

2. Experimental

2.1. Characterizations of materials

rGO and aMEGO were obtained from Sixth Element (Changzhou) Material Technology, Inc., and YP50F from Kuraray Inc. (Japan). These carbon materials were characterized with Fourier transform infrared spectroscopy (FTIR, attenuated total reflection mode, Thermo Nicolet nexus-470, US), X-ray diffraction (XRD) with Cu Kα radiation (λ=1.5406 Å, tube voltage 40 kV, tube current 30 mA, Rigaku SmartLab, Japan), Raman microscopy (LabRAM, RM3000, Renishaw, UK) with 532 nm laser and X-ray photoelectron spectroscopy (XPS, Thermo ESCALAB 250, US) with Al Kα radiation (hν = 1486.6 eV). Argon adsorption isotherms were carried out with Quantachrome Nova 2000 (Quantachrome, USA) at 87.3 K. The films made of these carbons were characterized with field-emission scanning electron microscopy (FESEM, FEI, Apreo, US). The contact angle of electrolytes on carbon films (1 cm×1 cm) was measured by an OCA 20 contact angle measurement system (Dataphysics, Germany). Electrical conductivity of the electrode films was measured using a 4-point probe method (Keithley, 4200-SCS, US).

2.2. Preparation of electrodes

To prepare electrodes of aMEGO or YP50F, 95 wt.% active material and 5 wt.% polytetrafluoroethylene (PTFE, 5 wt.% water solution) was mixed into a paste using a mortar and pestle, rolled into membranes with uniform thickness. The rGO membranes were prepared by rolling the paste mixture of 80 wt.% rGO, 10 wt.% conductive acetylene black and 10 wt.% PTFE. All the membranes were punched into circular electrodes with a diameter of 1 cm after drying overnight at 100 °C under vacuum. The typical weight/volume density/areal density of a 30 μm thick electrode is about 2 mg/0.85 g cm^{-3}/2.6 mg cm^{-2}, 2 mg/0.85 g cm^{-3}/2.6 mg cm^{-2} or 1 mg/0.42 g cm^{-3}/1.3 mg cm^{-2}, for aMEGO, YP50F or rGO, respectively. As a control, YP50F, aMEGO and rGO powers were also thoroughly mixed with a mass ratio of 2:2:1 and rolled into films following the preparation method of aMEGO or YP50F electrodes, denoted as *H3*. *H3* electrode and three-layer stacking electrodes of YP50F, aMEGO and rGO have a similar thickness of 90 μm, mass of 5 mg, density values of 0.71 g cm^{-3} and 6.4 mg cm^{-2}. As shown in Figure S1, the stacking electrodes are named following the layer sequence of near the current collector, in the middle and exposed to the separator. For example, a three-layer stacking film with YP50F, rGO and aMEGO sequentially arranged from current collector to separator is denoted as *YRA*. Two-layer stacking samples are named in the same way.

All testing electrodes were prepared into CR2032 cells in a glovebox with $O_2 < 0.1$ ppm and $H_2O < 0.1$ ppm with a symmetric two-electrode setup. Polypropylene diaphragm (PP) membrane (25 μm) was used as the separator and carbon coated aluminum foils (20 μm) used as current collectors. A stainless-steel spring was used to maintain the good electric contact between electrode with current collector. 1 M tetraethylammonium-tetrafluoroborate in acetonitrile ($TEABF_4$/AN), 1 M $TEABF_4$ in propylene carbonate ($TEABF_4$/PC) or 1 M ethyl-methylimmidazolium-tetrafluoroborate in acetonitrile ($EMIMBF_4$/AN) was used as electrolyte separately. Cyclic voltammetry (CV), galvanostatic charge and discharge (GCD), and electrochemical impedance spectroscopy (EIS) tests were conducted on a PARSTAT MC electrochemical workstation (Princeton Company, USA). EIS was carried out in a frequency range of 100 to 10 mHz with an alternating current perturbation of 10 mV.

2.3. Electrochemical data analysis

The specific capacitance was calculated from the discharge curves according to the following equations:

$$Cg = 4\frac{I\,\Delta\,t}{m\,\Delta V}$$

$$C_v = C_g\rho_v$$

and $C_s = C_g\rho_s$,

where C_g is the specific gravimetric capacitance of the single electrode (F g^{-1}), I is the constant charge/discharge current (A), Δt is the discharge time (s), m is the mass for two carbon electrodes (g) in a cell and ΔV is the voltage difference (V) in discharge. C_v, C_s, ρ_v and ρ_s are the specific volumetric capacitance (F cm^{-3}), the specific areal capacitance (F cm^{-2}), the volumetric density (g cm^{-3}) and the areal density (g cm^{-2}), respectively.

The specific energy density (E, Wh) and specific power density (P, W) were calculated using the following equations:

$$E = \frac{1}{2}CV^2,$$

and $$P = \frac{E}{t},$$

where V (V) is the cell voltage and t (h) is the discharge time.

The Warburg coefficient (σ) was calculated according to the following equations:

$$Z = |Z'| + |Z''|\ ,$$

$\omega\pi = 2f$,

and $Z'' = R + \sigma\omega^{-1/2}$,

where Z' and Z'' are the real and imaginary parts of the impedance, respectively; f is frequency in Hz and ω the radial frequency ($2\pi f$).

The complex form of capacitance C (ω) depends on the real part C' (ω) and the imaginary part C'' (ω), the latter of which is related to the loss of energy dissipation and frequency according to

$$C = \frac{-1}{2\pi f Z''} \text{ and } |C| = |C'| + |C''| .$$

3. Results and discussion

The structural and chemical characterizations of three carbons are shown in Figure S2. The XRD patterns show that YP50F and aMEGO have a typical porous structure, indicated by the high scattering intensity in the small angles, while rGO shows a layered structure with a graphitic peak at ~26°. The high I_D/I_G intensity ratio in Raman spectra show they are full of disorders and defects. The FTIR and XPS spectra indicate that the samples have certain oxygen groups with several percentages of oxygen in number of atoms.

The pore structures of aMEGO, YP50F and rGO analyzed by argon adsorption/desorption isotherms performed at 87.3 K are shown in Fig. 1a. From the isotherms of aMEGO and YP50F, we can see an obvious steep uptake at $P/P_0 < 0.01$ and a H3 hysteresis loop (defined by IUPAC) at high pressure region ($P/P_0 > 0.4$), indicating that aMEGO and YP50F have a microporous structure with mesopores. In contrast, rGO exhibits a mixture of Type-I and Type-IV isotherms with a H3 hysteresis loop, showing the co-existence of mesopores and macropores. Calculated with the density functional theory (DFT) method, the SSA is 2836.5, 1773.8 or 467.6 $m^2\ g^{-1}$ for aMEGO, YP50F or rGO, respectively. Pore size analysis has been carried out with a hybrid nonlocal DFT kernel, leading to distribution curves shown in Fig. 1b. Different from the continuous yet broad peaks of rGO in the width range of interest, YP50F or aMEGO has distinct characteristic peaks mainly corresponding to pores smaller than 3 nm or 9 nm, respectively. The cumulative pore volume (Fig. 1c) further shows that the pore volume of YP50F and aMEGO drastically increases at pore width of 3 nm or 9 nm, respectively, while the pore volume of rGO accumulates continuously. Detailed pore features are listed in Table S1. Based on the pore features, the fraction of pores with size smaller than 2 nm, 2–10 nm and 10–45 nm is respectively summarized in Fig. 1d. Clearly, aMEGO has a dominant pore size distribution at 2–10 nm, which accounts for 72.1% of the total pore volume. YP50F is composed of 65.7% pores in the width range of 0.5–2 nm and 25.2% pores in the width range of 2–10 nm. rGO exhibits a broad pore size distribution in 10–45 nm, which occupies 80.2% of the total pore volume. From the analysis, we can define the dominant pores in YP50F, aMGEO or rGO are micropores, small mesopores or large mesopores, respectively.

To investigate the effects of heterogeneous structure on the ionic behavior, EIS has been firstly performed on two-layer stacking electrodes made of two of aMEGO, rGO or YP50F membranes with a thickness of 50 μm for each. From the Nyquist plots shown in Fig. 2, we can get the series resistance (R_s), which is related to the internal wettability of electrolyte on the electrode, the conductivity of electrode material and the assembly of device [29]. The transfer resistance (R_t) corresponding to the semicircle, may come from the sum of the interfacial resistance between electrode and electrolyte and the contact resistance between electrode and current collector [30]. The 45° region has been considered as a consequence of equivalent distributed

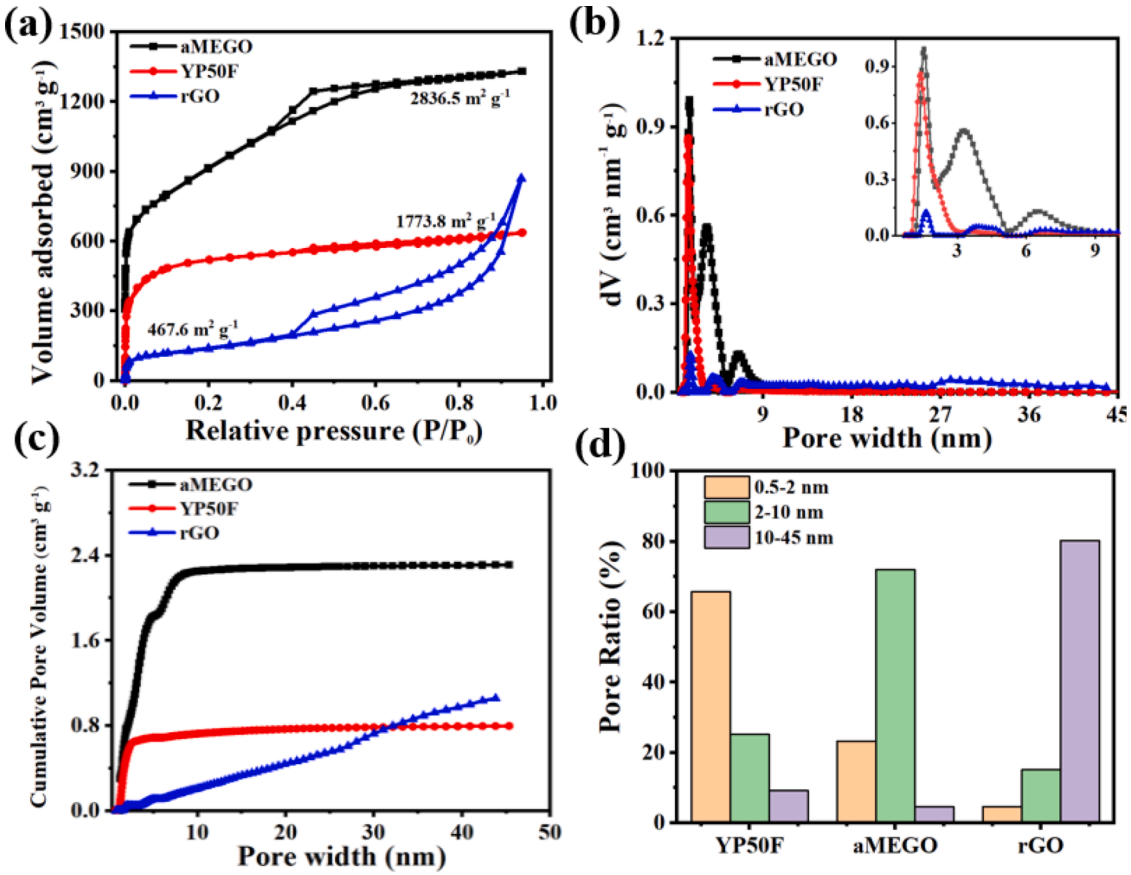

Fig. 1. Pore feature characterizations of three carbons. (a) Ar adsorption/desorption isotherms; (b) Pore size distributions with inset showing the enlarged data below 10 nm; (c) Cumulative pore volume and (d) fraction of pores in different ranges of widths.

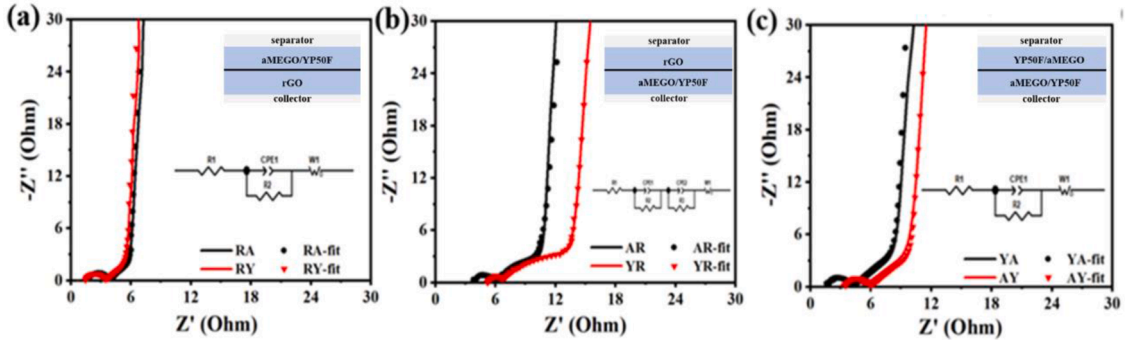

Fig. 2. Nyquist plots of symmetrical cells based on (a) *RA* and *RY*; (b) *AR* and *YR*; (c) *YA* and *AY* in $EMIBF_4$/AN (Inset images: schematic structures and equivalent circuits).

resistance (EDR) in a porous electrode, which is associated with the ionic diffusion in pores [31]. In the heterogenous stacking films, the ionic diffusion is largely influenced by the ionic path especially the interface between carbons with different pore features. From the impedance spectra, we can see that all the Nyquist plots display a characteristic semicircle at high-frequency range related to R_s and R_t, a nearly ideal 45° line at intermediate frequencies and an inclined line closed to 90° in the low-frequency region.

Among six sequences for two-layer stackings, stackings of *RA* and *RY* with rGO nearby the current collector shows the best ionic dynamics with similar R_s, R_t and EDR values, as shown in Fig. 2a. From the equivalent circuit simulation, we can determine a single ionic interface in the stacking. In contrast, when rGO layer is placed nearby the separator, *e.g.*, in *AR* or *YR* stacking, R_s and R_t increase and the plot at 45° is significantly elongated, as shown in Fig. 2b. The increased EDR suggests that the ionic transport path is hampered. Two resistances (R_2 and R_3) have to be used to fit the semicircle loop and the distorted 45° line in *AR* or *YR*. The comparison between Figures 2a and 2b indicates that, rGO with large mesopores benefits the ionic transport under the electrode polarization when being buried inside the electrode. In contrast, when rGO is exposed to the separator, as in *AR* or *YR*, the ionic transport is probably hampered by the 'blocking' of ions across the aMEGO/YP50F and rGO interface. In Fig. 2b, *AR* shows the better ionic dynamics compared to *YR*, which may be explained by the larger SSA and pore size of aMEGO. In addition, when aMEGO and YP50F are stacked (Fig. 2c), the ionic dynamics of the heterogenous electrode is similar for *YA* or *AY* with comparable R_t and EDR; R_s of *YA* is slightly smaller than that of *AY*, possibly due to the higher electric conductivity of YP50F (Figure S3).

Based on the EIS results, molecular dynamics (MD) simulations were performed by comparing different two-layer stackings to understand the ionic transport across the heterogeneous layers (Figure S4a). Figure S4b-d clearly indicate the higher ionic transport efficiency when the larger pores are buried inside the electrode (Model 2), in contrast to the accumulation of abundant ions at the interface when the smaller pores are inside (Model 1) [32, 33]. Finite element simulations were also carried out to simulate the ionic diffusion for three-layer stackings, as

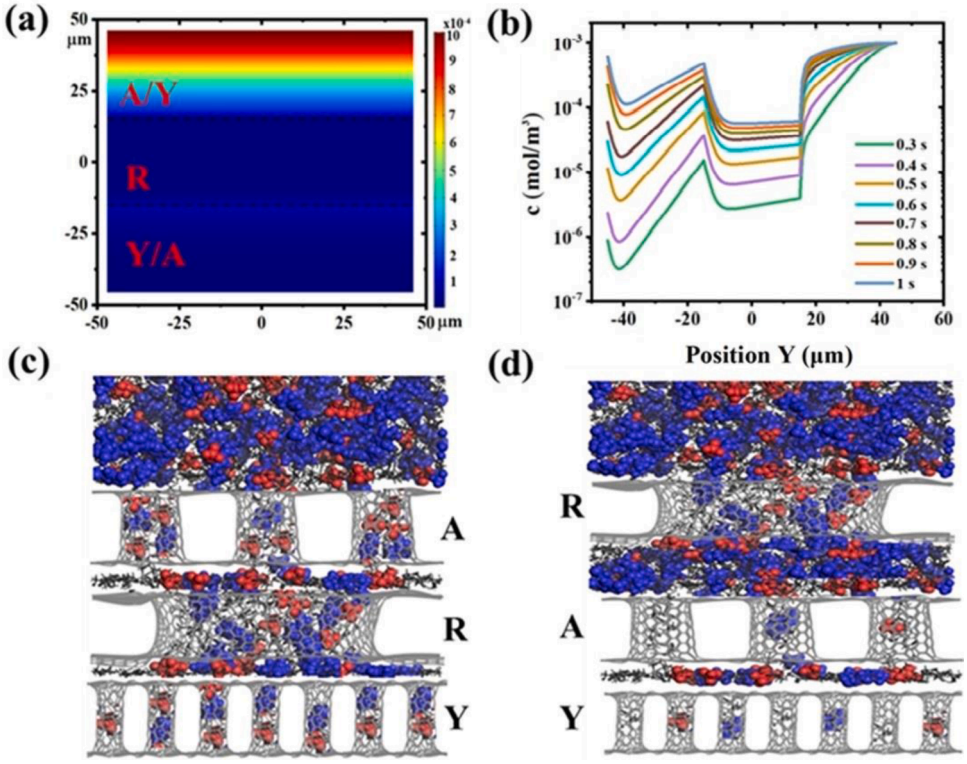

Fig. 3. (a) Simulated concentration distribution of ions for *YRA* or *ARY* configuration after charging for 0.5 s; (b) Concentration evolution along the thickness direction for *YRA* or *ARY* with charging time; Schematic of ions distribution in (c) *YRA* or (d) *YAR*.

shown in Figure S5. In the modeling, the diffusion rate of three carbons was assumed as in an order of rGO > aMEGO = YP50F to highlight the effect of position of rGO in the stackings. As shown in Figures 3a and 3b, when rGO is placed in the middle, *e.g.*, in YRA or ARY, the simulated ion distribution shows no ion accumulation at the interfaces, and the ion concentration reaches a reasonably high value after charging for 1 s. In contrast, an ion blocking is observed inside the electrode for the other two situations, leading to the relatively low ion concentrations (Figure S6). The simulations indicate the efficient ionic transport of rGO when being placed in the middle, especially when the layer nearby electrolyte can adsorb enough ions for the following diffusion, as schematically shown in Fig. 3c [34–36]. In contrast, an ion aggregation between rGO and aMEGO/YP50F layers is formed when rGO is directly exposed to the electrolyte, leading to a sluggish ionic transport (Fig. 3d).

Based on the results above, a proper design of stacking orders should be able to improve the performance of stacking electrodes of three layers. The SEM images in Figure S7 clearly show the interface in the stacking, as three carbons have different density, morphology and pore features. In the following three groups of samples with a similar thickness of 90 μm are compared, *i.e., Group I*: membranes made of single carbons (YP50F, aMEGO, rGO) or their uniform mixture (*H3*), *Group II*: six stacking electrodes of three different layers (*YRA, ARY, RYA, AYR, YAR, RAY*), and *Group III*: three-layer stackings with rGO in the middle while another carbon on both sides (*ARA, YRY*). The CV curves measured at 200 mV s^{-1} in Figures S8a-S8c demonstrate quasi-rectangle shapes and the GCD measurements carried out at 1 A g^{-1} in Figures S8d-S8f show triangle charge/discharge curves for all 12 samples in 1 M $EMIMBF_4$/AN electrolyte till a voltage of 2.7 V, indicating the nearly ideal capacitive behavior of all the electrodes. Specific capacitance values have been calculated from a systematic GCD testing performed at currents till 20 Ag^{-1} (Figure S9), summarized in Fig. 4a. From the data of gravimetric capacitances, we can see the following trends: 1) *Group I* samples, except for *H3*, generally have the lower specific capacitances for the electrode thickness of 90 μm. Electrodes made of rGO only give a capacitance value of 71 F g^{-1} at 1 A g^{-1}; 2) *Group II* samples spread in a wide range, but two samples with rGO in the middle (*YRA, ARY*) demonstrate the best capacitances among all the six stackings of three different carbon layers. At 1 A g^{-1}, *YRA* and *ARY* show similar specific capacitance values above 200 F g^{-1}, higher than *H3* (190.7 F g^{-1}); 3) With rGO in the middle, replacing YP50F with aMEGO (leading to *ARA*) or replacing aMEGO with YP50F (leading to *YRY*) based on *YRA* or *ARY* has resulted in the deteriorated performance, but *ARA* shows much higher values than *YRY*.

The comparison has demonstrated the advantage of heterogeneous electrode design, especially when rGO is buried inside the electrode. It worth noting that, although *ARY* and *YRA* have similar capacitances at 1 A g^{-1}, *ARY* shows more significant degradation at high currents than *YRA*, highlighting the importance of aMEGO when being placed nearby the separator. On the other hand, the lower capacitance of *ARA* compared to *YRA* indicates the necessity for the existence of YP50F, especially when being placed nearby the current collector. This could be explained by the higher electric conductivity of YP50F, consistent to the EIS measurement of two-layer stackings. Interestingly, *H3* electrode made by uniformly mixing the three carbons in the slurry shows the better performance than the electrodes made of single type of carbons, verifying the effect of heterogeneous structure even on the micrometer scale, which has led to the relatively smaller R_s, R_t and EDR values compared to the single types of carbons, as shown in EIS results in Fig. 4b and the fittings in Figure S10a. *H3* also shows the highest electrical conductivity among all the electrodes (Figure S3). From Fig. 4b, we again see the role of rGO in the middle, leading to generally the lowest ionic resistance among all the samples. Specifically, when rGO is placed in the middle layer, a single interface is formed, as can be seen from the curves and fittings for *YRA/ARY* and *ARA/YRY*, in Figures S10b and S10c. In contrast, two semicircles have been identified from *AYR/RYA* and *YAR/RAY* stacking electrodes (Figure S10d).

The Bode plots are shown in Figures 4c and 4d, in which shift to the higher frequency of C′ or the shorter dielectric relaxation time (1/f, τ_0) in C″ suggests the quick response of ions under polarization [37, 38]. From the plots we can see that, *YRA* or *ARY* shows the faster polarization

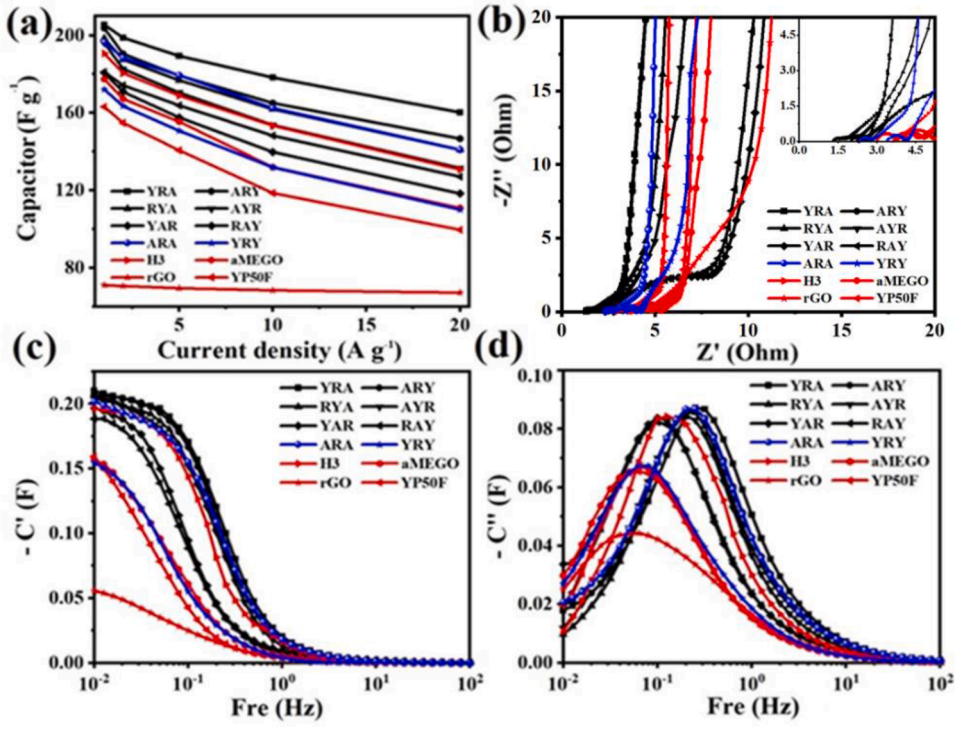

Fig. 4. Electrochemical characterizations of 12 different three-layer stacking electrodes in $EMIBF_4$/AN: (a) Specific gravimetric capacitances at different current densities; (b) Nyquist plots with inset showing the enlarged view in the range of high frequencies; (c) Real capacitance and (d) imaginary capacitance plots.

at highest frequencies and the smallest τ_0 among all the electrodes. The polarization equilibration of *ARA* is obviously faster than *YRY*. The faster equilibration of the polarization for *H3* electrode again shows the promising design of microscopic heterogeneous structure, which deserves further investigations in the future.

The EDLC performances of 90 μm thick electrodes made of three-layer stackings have also been measured in 1 M $TEABF_4$/AN or $TEABF_4$/PC electrolyte, with the electrodes made of single types of carbons or *H3* as contrast. From the CV and GCD data shown in Figures S11 and S12, we can identify the similar trends as obtained in 1 M $EMIBF_4$/AN, with the best performances from *YRA* stacking. Figures S13 shows the faster ionic dynamics of *YRA* and of *H3* compared to the stacking electrodes and the single type of carbons. The gravimetric capacitance of 90 μm thick *YRA* electrodes measured as 1 A g^{-1} is 176.7 or 200.6 F g^{-1} in $TEABF_4$/AN or $TEABF_4$/PC, respectively. The different performances of these electrodes in different electrolytes could be related to their different wetting situations, as exampled in the contact angle measurement in Figure S14a. From the statistics of contact angles in Figure S14b, we can see that $TEABF_4$/PC shows the best wetting among three electrolytes studied. Very interestingly, when rGO is buried in the middle, the contact angle of *YRA* or *ARY* are smaller than aMEGO or YP50F, respectively.

The heterogeneous stacking design may provide us a good opportunity to further optimize the performance towards even thicker electrodes or higher mass loading, as it is considered a challenge to realize both high volumetric and areal capacitances [39]. Films made of aMEGO, rGO or YP50F with 70 μm for each have been stacked in *YRA* configuration and tested in 1 M $EMIMBF_4$/AN. The thickness, mass and density per electrodes is ~210 μm, ~10 mg, and ~0.61 g cm^{-3}/~12.7 mg cm^{-2}. Figures 5a and 5b show that the thick electrode maintains the double-layer capacitance behavior, indicated by the quasi-square CV curves and quasi-triangle charge/discharge curves. The gravimetric, volumetric and areal capacitance of *YRA* at 1 A g^{-1} is 171.4 F g^{-1}, 102.8 F cm^{-3} and 2.2 F cm^{-2}, which remains 118.8 F g^{-1},102.8 F cm^{-3} and 1.5 F cm^{-2} at 20 A g^{-1}, respectively. The electrode possesses a retention of 90.21% and nearly 100% columbic efficiency after 20,000 cycles tested at a current density of 10 A g^{-1}, implying good cycling stability (Fig. 5d). As shown in Fig. 5c, we can see volumetric and areal capacitance of *YRA* are much higher than the single types of carbon *H3* (Figure S15) and many other carbon-based electrodes with the similar thicknesses tested under comparable conditions (listed in Table S2). As the thickness (210 μm) and density (0.61 g cm^{-3}) of *YRA* electrode is close to the electrode parameters in practical applications, the energy density of 43.4 W h Kg^{-1} (at 1 A g^{-1}) could lead to a practically useful device energy of above 13 W h Kg^{-1} if we presume the active material occupy 30 wt.% it the device [11,40].

4 Conclusion

In this work, we have designed a series of heterogeneous electrodes by stacking different carbon films which own different pore size distributions. A comprehensive comparison has led to our cognition regarding the efficient ionic transport of rGO inside the stacking. Combining the sufficient supply from aMGEO due to the high SSA, the electrochemical performance of the stacking films has been optimized. The three-layer stacking electrodes with a thickness of 210 μm, following the stacking sequence of YP50F, rGO and aMEGO, have shown a gravimetric capacitance of 171.4 F g^{-1}, volumetric capacitance of 102.8 F cm^{-3} and areal capacitance of 2.2 F cm^{-2} in 1 M $EMIBF_4$/AN electrolyte at a voltage of 2.7 V. Such a strategy may open more opportunities for improving the supercapacitance of thicker or high mass loading electrodes.

Author statement

I have made substantial contributions to the conception or design of the work; or the acquisition, analysis, or interpretation of data for the work; And I have drafted the work or revised of data for the work; And I

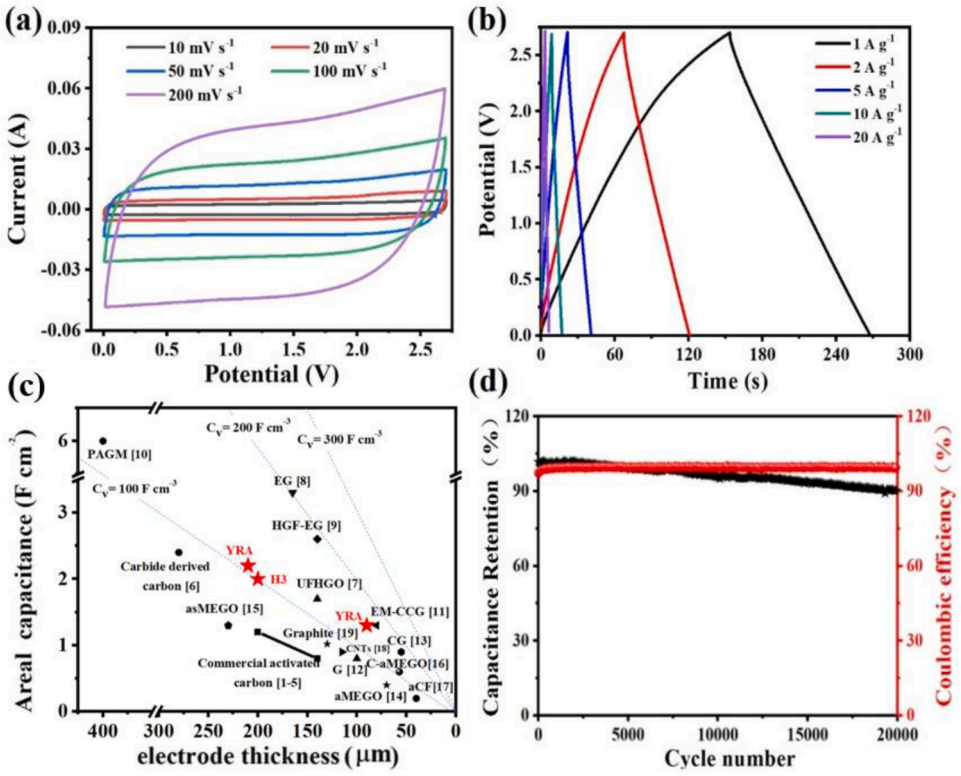

Fig. 5. Electrochemical performances of 210 μm thick *YRA* electrodes in $EMIBF_4$/AN: (a) CV curves at various scan rates; (b) GCD curves at different currents; (c) Areal capacitance comparison with reported electrode materials with the thickness and (d) cycling stability of YRA electrode at 10 A g^{-1}.

have approved the final version to be published; And I agree to be accountable for all aspects of the work in ensuring that questions related to the accuracy or integrity of any part of the work are appropriately investigated and resolved.

All persons who have made substantial contributions to the work reported in the manuscript, including those who provided editing and writing assistance but who are not authors, are named in the Acknowledgments section of the manuscript and have given their written permission to be named. If the manuscript does not include Acknowledgments, it is because the authors have not received substantial contributions from nonauthors.

Declaration of Competing Interest

The authors declare that they have no known competing financial interests or personal relationships that could have appeared to influence the work reported in this paper.

Data Availability

No data was used for the research described in the article.

Data availability

Data will be made available on request.

Acknowledgments

We appreciate funding support from the National Natural Science Foundation of China (grant Nos. 51322204 and 51772282). The authors thank The Sixth Element (Changzhou) Materials Technology, Inc. for providing rGO and aMEGO. The authors appreciate the help from Xingcheng Li for contact angles data collection.

Supplementary materials

Supplementary material associated with this article can be found, in the online version, at doi:10.1016/j.ensm.2022.05.020.

References

[1] C.G. Zhang, H.Z. Du, K. Ma, Z.H. Yuan, Ultrahigh-Rate Supercapacitor Based on Carbon Nano-Onion/Graphene Hybrid Structure toward Compact Alternating Current Filter, Adv. Energy Mater. 10 (2020), 2002132.
[2] Z.H. Pan, H.Z. Zhi, Y.C. Qiu, J. Yang, L.D. Xing, Q.C. Zhang, X.Y. Ding, X.S. Wang, G.C. Xu, H. Yuan, M. Chen, W.F. Li, Y.G. Yao, N. Motta, M.N. Liu, Y.G. Zhang, Achieving commercial-level mass loading in ternary-doped holey graphene hydrogel electrodes for ultrahigh energy density supercapacitors, Nano Energy 46 (2018) 266–276.
[3] Q. Li, Z.W. Dai, J.B. Wu, W. Liu, T. Di, R. Jiang, X. Zheng, W.Z. Wang, X.X. Ji, P. Li, Z.H. Xu, X.P. Qu, Z.M. Xu, J. Zhou, Fabrication of Ordered Macro-Microporous Single-Crystalline MOF and Its Derivative Carbon Material for Supercapacitor, Adv. Energy Mater. 10 (2020), 1903750.
[4] C. Schütter, S. Pohlmann, A. Balducci, Industrial Requirements of Materials for Electrical Double Layer Capacitors: impact on Current and Future Applications, Adv. Energy Mater. 9 (2019), 1900334.
[5] H.T. Sun, J. Zhu, D. Baumann, L.L. Peng, Y.X. Xu, I. Shakir, Y. Huang, X.F. Duan, Hierarchical 3D electrodes for electrochemical energy storage, Nat. Rev. Mater. 4 (2018) 45–60.
[6] J.W. Han, W. Wei, C. Zhang, Y. Tao, W. Lv, G.W. Ling, F.Y. Kang, Q.H. Yang, Engineering Graphenes from the Nano- to the Macroscale for Electrochemical Energy Storage, Electrochem. Energy Rev. 1 (2018) 139–168.
[7] F. Beguin, V. Presser, A. Balducci, E. Frackowiak, Carbons and electrolytes for advanced supercapacitors, Adv. Mater. 26 (2014) 2219–2251.
[8] Y. Chen, X.Y. Hao, G.Z. Chen, Nanoporous Versus Nanoparticulate Carbon-Based Materials for Capacitive Charge Storage, Energy Environ. Mater. 3 (2020) 247–264.
[9] W.J. Tian, H.Y. Zhang, X.J. Duan, H.Q. Sun, G.S. Shao, S.B. Wang, Porous Carbons: structure-Oriented Design and Versatile Applications, Adv. Funct. Mater. 30 (2020), 1909625.
[10] Y. Gogotsi, P. Simon, True Performance Metrics in Electrochemical Energy Storage, Science 334 (2011) 917–918.
[11] P. Simon, Y. Gogotsi, Perspectives for electrochemical capacitors and related devices, Nat. Mater. 19 (2020) 1151–1163.
[12] J.L. Ye, P. Simon, Y.W. Zhu, Designing ionic channels in novel carbons for electrochemical energy storage, Natl. Sci. Rev. 7 (2020) 191–201.
[13] S.L. Wu, Y.W. Zhu, Highly densified carbon electrode materials towards practical supercapacitor devices, Sci. China Mater. 60 (2016) 25–38.
[14] Y.H. Kim, B.H. Park, Y.J. Choi, G.W. Lee, H.K. Kim, K.B. Kim, Compact graphene powders with high volumetric capacitance: microspherical assembly of graphene via surface modification using cyanamide, Energy Storage Mater 24 (2020) 351–361.
[15] H. Li, Y. Tao, X.Y. Zheng, J.Y. Luo, F.Y. Kang, H.M. Cheng, Q.H. Yang, Ultra-thick graphene bulk supercapacitor electrodes for compact energy storage, Energy Environ. Sci. 9 (2016) 3135–3142.
[16] Z. Li, S. Gadipelli, H. Li, C.A. Howard, D.J.L. Brett, P.R. Shearing, Z. Guo, I. P. Parkin, F. Li, Tuning the interlayer spacing of graphene laminate films for efficient pore utilization towards compact capacitive energy storage, Nat. Energy 5 (2020) 160–168.
[17] W. Guo, C. Yu, S.F. Li, J.S. Qiu, Toward commercial-level mass-loading electrodes for supercapacitors: opportunities, challenges and perspectives, Energy Environmen. Sci. 14 (2021) 576–601.
[18] J. Chmiola, G. Yushin, Y. Gogotsi, C. Portet, P. Simon, P.L. Taberna, Anomalous Increase in Carbon Capacitance at Pore Sizes Less Than 1 Nanometer, Science 313 (2006) 1760–1763.
[19] H. Zhang, G.P. Cao, Y.S. Yang, Z.N. Gu, Capacitive performance of an ultralong aligned carbon nanotube electrode in an ionic liquid at 60 °C, Carbon N Y 46 (2008) 30–34.
[20] E. Frackowiak, Q. Abbas, F. Béguin, Carbon/carbon supercapacitors, J. Energy Chem. 22 (2013) 226–240.
[21] J. Gao, W. Guo, D. Feng, H.T. Wang, D.Y. Zhao, L. Jiang, High-performance ionic diode membrane for salinity gradient power generation, J. Am. Chem. Soc. 136 (2014) 12265–12272.
[22] J. Xiao, H.L. Zhan, X. Wang, Z.Q. Xu, Z.Y. Xiong, K. Zhang, G.P. Simon, J.Z. Liu, D. Li, Electrolyte gating in graphene-based supercapacitors and its use for probing nanoconfined charging dynamics, Nat. Nanotechnol. 15 (2020) 683–689.
[23] Y.H. Zhou, L. Jiang, Bioinspired Nanoporous Membrane for Salinity Gradient Energy Harvesting, Joule 4 (2020) 2244–2248.
[24] S. Kondrat, P. Wu, R. Qiao, A.A. Kornyshev, Accelerating charging dynamics in subnanometre pores, Nat. Mater. 13 (2014) 387–393.
[25] J.W. Han, H. Li, Q.H. Yang, Compact energy storage enabled by graphenes: challenges, strategies and progress, Mater. Today 51 (2021) 552–565.
[26] A. Bianco, Y. Chen, E. Frackowiak, M. Holzinger, N. Koratkar, V. Meunier, S. Mikhailovsky, M. Strano, J.M.D. Tascon, M. Terrones, Carbon N Y 161 (2020) 373–391.
[27] P. Li, T.X. Shang, X.M. Dong, H. Li, Y. Tao, Q.H. Yang, A Review of Compact Carbon Design for Supercapacitors with High Volumetric Performance, Small (2021), e2007548.
[28] A.C. Forse, J.M. Griffin, C. Merlet, P.M. Bayley, H. Wang, P. Simon, C.P. Grey, NMR Study of Ion Dynamics and Charge Storage in Ionic Liquid Supercapacitors, J. Am. Chem. Soc. 137 (2015) 7231–7242.
[29] B.A. Mei, O. Munteshari, J. Lau, B. Dunn, L. Pilon, Physical Interpretations of Nyquist Plots for EDLC Electrodes and Devices, J. Phys. Chem. C 122 (2017) 194–206.
[30] R. He, S.l. Chen, F. Yang, B.L. Wu, Dynamic Diffuse Double-Layer Model for the Electrochemistry of Nanometer-Sized Electrodes, J. Phys. Chem. B 110 (2006) 3262–3270.
[31] L.X. Fan, Y.W. Liu, J.W. Xiong, H.S. White, S.L. Chen, Electron-Transfer Kinetics and Electric Double Layer Effects in Nanometer-Wide Thin-Layer Cells, ACS Nano 8 (2014) 10426–10436.
[32] Y.W. Liu, S.L. Chen, Theory of Interfacial Electron Transfer Kinetics at Nanometer-Sized Electrodes, J. Phys. Chem. C 116 (2012) 13594–13602.
[33] J. Huang, Y. Gao, J. Luo, S.S. Wang, C.K. Li, S.L. Chen, J.B. Zhang, Editors' Choice—Review—Impedance Response of Porous Electrodes: theoretical Framework, Physical Models and Applications, J. Electrochem. Soc. 167 (2020), 166503.
[34] S. Bi, H. Banda, M. Chen, L. Niu, M.Y. Chen, T.Z. Wu, J.S. Wang, R.X. Wang, J. M. Feng, T.Y. Chen, M. Dinca, A.A. Kornyshev, G. Feng, Molecular understanding of charge storage and charging dynamics in supercapacitors with MOF electrodes and ionic liquid electrolytes, Nat. Mater. 19 (2020) 552–558.
[35] J. Huang, J.B. Zhang, Theory of Impedance Response of Porous Electrodes: simplifications, Inhomogeneities, Non-Stationarities and Applications, J. Electrochem. Soc. (163) (2016) A1983–A2000.
[36] A. Bianco, Y. Chen, E. Frackowiak, M. Holzinger, N. Koratkar, V. Meunier, S. Mikhailovsky, M. Strano, J.M.D. Tascon, M. Terrones, Carbon science perspective in 2020: current research and future challenges, Carbon N Y 161 (2020) 373–391.
[37] L. Borchardt, D. Leistenschneider, J. Haase, M. Dvoyashkin, Revising the Concept of Pore Hierarchy for Ionic Transport in Carbon Materials for Supercapacitors, Adv. Energy Mater. 8 (2018), 1800892.

[38] H.D. Yoo, J.H. Jang, J.H. Ryu, Y. Park, S.M. Oh, Impedance analysis of porous carbon electrodes to predict rate capability of electric double-layer capacitors, J. Power Sources 267 (2014) 411–420.
[39] W.S. Chen, J.J. Gu, Q.L. Liu, M.Z. Yang, C. Zhan, X.N. Zang, T. Anh Pham, G.X. Liu, W. Zhang, D. Zhang, B. Dunn, Y.M. Wang, Two-dimensional quantum-sheet films with sub-1.2 nm channels for ultrahigh-rate electrochemical capacitance, Nat. Nanotechnol. (2021), https://doi.org/10.1038/s41565-021-01020-0.
[40] Y.W. Zhu, S. Murali, M.D. Stoller, K.J. Ganesh, W.W. Cai, P.J. Ferreira, A. Pirkle, R. M. Wallace, K.A. Cychosz, M. Thommes, E.A.Stach D.Su, R.S. Ruoff, Carbon-based supercapacitors produced by activation of graphene, Science 332 (2011) 1537–1541.